

Probing Majorana-like states in quantum dots and quantum rings

Benedikt Scharf and Igor Žutić

Department of Physics, University at Buffalo, State University of New York, Buffalo, NY 14260, USA

(Dated: October 17, 2018)

Engineering chiral p -wave superconductivity in semiconductor structures offers fascinating ways to obtain and study Majorana modes in a condensed matter context. Here, we theoretically investigate chiral p -wave superconductivity in quantum dots and quantum rings. Using both analytical as well as numerical methods, we calculate the quasiparticle excitation spectra in these structures and the corresponding excitation amplitudes and charge densities. In the topological regime, we can observe the chiral edge modes localized at the boundaries and possessing finite energy in quantum dots and quantum rings. By applying a magnetic field which is expelled from the quantum ring, but which creates a flux that is an odd integer multiple of $\Phi_0/2 = \pi\hbar/e$, Majorana modes, that is, (approximately) degenerate edge modes with zero energy and zero charge density, become possible in the topological regime. Furthermore, we investigate finite-size effects that split these degenerate edge modes as well as the effect of a magnetic field penetrating into the superconducting region that can under certain circumstances still support edge modes with approximately zero energy and charge.

PACS numbers: 74.78.Na, 74.25.Ha, 74.45.+c

Keywords: Majorana modes, quantum dots, quantum rings

I. INTRODUCTION

Originally proposed almost eight decades ago, Majorana fermions are their own antiparticles, unlike, for example, electrons and their positronic counterparts.¹ While in high-energy physics the concept of Majorana fermions remains important, albeit not experimentally demonstrated yet,² the search for Majorana fermions in condensed-matter systems has developed into a topic of immense research interest in recent years.^{3–8} The attraction of pursuing Majorana fermions in solid-state systems is twofold: First, setups exhibiting Majorana modes could be more easily tailored in such systems. Secondly, Majorana fermions in a solid-state context are governed by non-Abelian statistics, which makes them potentially useful for topological quantum computation.^{9,10}

In contrast to high-energy physics, where Majorana fermions are proposed to be fundamental particles, Majorana fermions in a solid-state context are emergent quasiparticle excitations. Since Majorana modes need to be their own antiparticles, superconductors offer a natural choice for systems in which to look for such excitations. The reason for this is that, in the Bardeen-Cooper-Schrieffer (BCS) theory of superconductivity, quasiparticle excitations are described by superpositions of both electrons and holes. Thus, excitations which are their own antiparticles, that is, excitations which are described by operators that are their own Hermitian conjugate, are possible at zero energy in certain types of superconductors. These superconductors, termed topological superconductors, possess a bulk pairing gap and—in their topologically nontrivial regime—gapless edge or surface states which can then under certain circumstances support Majorana fermions as midgap states (see Fig. 1).^{11–13}

In order to realize Majorana fermions in condensed-

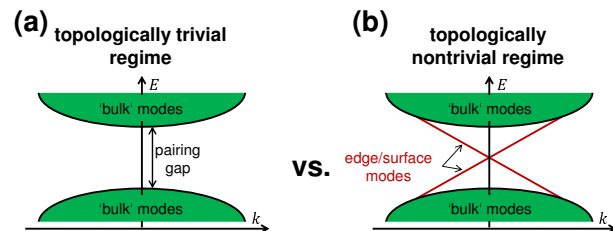


FIG. 1. (Color online) Excitation spectrum of a topological superconductor in the (a) trivial and (b) nontrivial regimes. By closing and subsequently reopening the pairing gap a transition between both regimes can be induced.

matter physics, it has long been proposed to utilize the midgap states of spinless chiral p -wave superconductors.^{14–20} While some superconducting materials such as Sr_2RuO_4 have been argued to possess a superconducting state with p -wave symmetry,^{21,22} it might be simpler to engineer p -wave pairing in more easily accessible systems. These proposals often, although not always, involve combining superconductivity, Zeeman splitting, and strong spin-orbit coupling,^{23–26} which makes the field of spintronics^{27,28} also relevant in this context. Typically, p -wave pairing is proximity-induced in materials with strong spin-orbit coupling, such as topological insulators²⁹ or semiconductors with strong Rashba coupling, by bringing them close to an s -wave superconductor. The Zeeman term then controls transitions between the topologically trivial and nontrivial regimes of the induced p -wave superconductor.

Proposals for such systems include the interface between a three-dimensional topological insulator and an s -wave superconductor, where Majorana modes can be bound to an Abrikosov vortex core,³⁰ or wires, either semiconductor wires with strong Rashba spin-orbit coupling^{31–33} or topological insulator wires,^{34,35} subject

to a magnetic field and brought in close proximity to an s -wave superconductor. Besides, it has been suggested that Majorana modes can appear in systems that are in proximity to an s -wave superconductor, but do not require the presence of spin-orbit coupling.^{36–39} Conversely, d -wave superconductors^{40,41} have been proposed as an alternative source for proximity-induced chiral p -wave pairing in Rashba or topological insulator structures with Zeeman splitting.^{42–45} Antiferromagnetically ordered chains of magnetic atoms on the surface of a conventional s -wave superconductor, where topologically unprotected Shiba states are converted into Majorana-bound states in a weak Zeeman field, offer another possible venue to Majorana modes.⁴⁶

A setup consisting of two quantum dots with applied noncollinear magnetic fields and connected by an s -wave superconductor has been suggested to support modes localized in the dots that exhibit most properties of Majorana modes, but that are not topologically protected.⁴⁷ Recent proposals to detect and control the Andreev reflection in topological insulator/superconductor/topological insulator⁴⁸ as well as in ferromagnet/superconductor⁴⁹ junctions indicate a possibly similar control of proximity-induced topological superconductivity, crucial for the appearance of Majorana modes.

Potential signatures of Majorana modes in the above systems are usually centered on the fact that Majorana modes can also affect transport and thermodynamic properties of the (induced) topological superconductors.^{50–65} Of all these proposals, the setup based on hybrid superconductor-semiconductor wire structures with Rashba spin-orbit coupling and Zeeman splitting^{31,32} has been the most prevalent until now, with experiments conducted in InSb^{66–68} and InAs^{69,70} semiconductor wires as well as ferromagnetic atomic chains.^{71,72} In these experiments, a zero-bias peak in the tunneling conductance has been observed, which potentially points to the presence of Majorana zero-energy modes.^{50–53} However, mechanisms which could also give rise to this zero-bias conductance peak in the absence of Majorana modes, such as Kondo physics,⁷³ strong disorder,^{74–76} smooth end confinement,⁷⁷ or boundary effects,⁷⁸ have been invoked. Moreover, experiments on semiconductor nanowire quantum dots strongly coupled to a conventional superconductor suggest that a zero-bias conductance anomaly with properties very similar to that expected for Majorana fermions can arise even without topological superconductivity.⁷⁹

Thus, until now the experimental evidence for Majorana modes remains inconclusive,^{80,81} although there are several proposals to supplement the tunneling conductance measurements in wires to verify the presence of Majorana-bound states or rule out some of the alternative sources for the zero-bias peak.^{82–85} Moreover, whereas disorder in chiral p -wave superconductor wires⁸⁶ is detrimental to the topological order supporting Majorana modes, disorder can even have a potentially stabi-

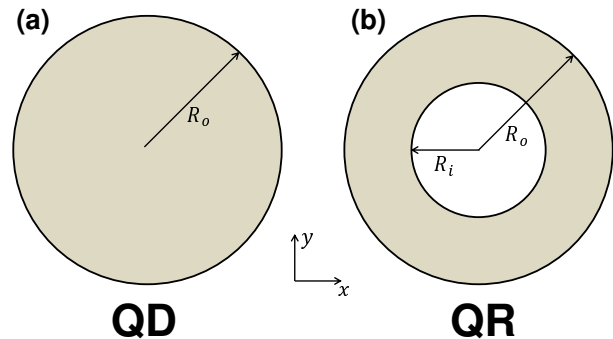


FIG. 2. (Color online) (a) QD and (b) QR considered in Sec. III A. The shaded areas are areas with p -wave superconductivity.

lizing effect in the hybrid superconductor-semiconductor wire structures studied experimentally.⁸⁷ Likewise, interaction effects in these hybrid structures are predicted to result in a reduction of the induced pairing gap,⁸⁸ but to actually expand the parameter range of the topologically nontrivial regime.⁸⁹

In contrast to these wire structures, we investigate the quasiparticle excitations, including possible Majorana modes, in quantum dots (QDs) and quantum rings (QRs) with (possibly induced) p -wave pairing. While there are several works on the ring geometry for the chiral p -wave superconductor and related models,^{17,62,63,90–93} our focus is on providing an in-depth analysis of the system and of the effects of finite size or magnetic fields penetrating into the superconducting region.

The paper is organized as follows: Section II introduces the effective model used to describe the QDs and QRs. The results obtained from this model are then presented in Sec. III, for QDs and QRs without any magnetic field (Sec. III A), QRs which enclose a magnetic flux, but which are not penetrated by a magnetic field (Sec. III B), and finally QRs into which a magnetic field can penetrate (Sec. III C). Section IV is devoted to the discussion of possible experimental realizations of the QDs and QRs as well as potential methods to distinguish Majorana modes from other phenomena. A brief summary in Sec. V concludes the paper.

II. MODEL AND METHODS

In this paper, we consider QDs of radius R_o and QRs of inner radius R_i and outer radius R_o confined to the xy plane and with chiral p -wave superconductivity (see Fig. 2). Apart from certain superconducting materials such as Sr_2RuO_4 , which has been argued to possess a state with p -wave symmetry, there are several proposals to engineer p -wave pairing in more easily accessible materials such as semiconductors with strong Rashba spin-orbit coupling by placing them close to an s -wave superconductor and exploiting proximity effects.⁹⁴ Since in

the latter setup a magnetic field can also penetrate into the QDs or QRs without being expelled, we allow for the presence of a constant magnetic field $\mathbf{B} = B\mathbf{e}_z$ inside the QDs or QRs.

As a model for the interior of the QD and QR we consider a two-dimensional spinless p -wave superconductor, which can be described by the Bogoliubov-de Gennes (BdG) Hamiltonian⁹⁵

$$\hat{H} = \begin{pmatrix} H_0(\mathbf{r}) & \Delta(\mathbf{r}) \\ \Delta^\dagger(\mathbf{r}) & -H_0^*(\mathbf{r}) \end{pmatrix} \quad (1)$$

in particle-hole space, where

$$H_0(\mathbf{r}) = \frac{[\hat{\mathbf{p}} + e\mathbf{A}(\mathbf{r})]^2}{2m^*} - E_F + V(r) \quad (2)$$

is the single-particle Hamiltonian and

$$\Delta(\mathbf{r}) = \alpha e^{-in_\Phi\theta} \{\hat{p}_x - eA_x(\mathbf{r}) - i[\hat{p}_y - eA_y(\mathbf{r})]\} \quad (3)$$

describes the pairing amplitude of the superconductor. Here, \mathbf{r} denotes the position in the xy plane, $\hat{\mathbf{p}}$ the momentum operator in the xy plane, $\mathbf{A}(\mathbf{r})$ the magnetic vector potential in the xy plane, m^* the electronic effective mass, E_F the Fermi energy, $V(r)$ a radially symmetric confinement potential in the xy plane, $\alpha = |\alpha|e^{i\varphi_\alpha}$ the p -wave pairing parameter, and $e = |e|$ the elementary charge. If a magnetic field is present, the p -wave pairing parameter acquires an additional phase of $-n_\Phi\theta$, where θ is the polar angular coordinate and n_Φ an integer related to the magnetic flux (see below). In the absence of a magnetic field, the sign of E_F determines whether the system described by Eq. (1) is in the topologically trivial regime ($E_F < 0$), where no edge modes appear, or in the topologically nontrivial regime ($E_F > 0$), where chiral edge modes can arise.

To model the confinement in the xy plane, we use polar coordinates (r, θ) and infinite hard-wall potentials

$$V(r) = \begin{cases} 0 & \text{for } r < R_o \\ \infty & \text{elsewhere} \end{cases} \quad (4)$$

and

$$V(r) = \begin{cases} 0 & \text{for } R_i < r < R_o \\ \infty & \text{elsewhere} \end{cases} \quad (5)$$

$$\begin{pmatrix} -\frac{\hbar^2}{2m^*} \left\{ \partial_r^2 + \frac{1}{r} \partial_r - \frac{[m+n(r)]^2}{r^2} \right\} - E_F & -i\hbar|\alpha| \left[\partial_r + \frac{m+1+n_\Phi-n(r)}{r} \right] \\ -i\hbar|\alpha| \left[\partial_r - \frac{m+n(r)}{r} \right] & \frac{\hbar^2}{2m^*} \left\{ \partial_r^2 + \frac{1}{r} \partial_r - \frac{[m+1+n_\Phi-n(r)]^2}{r^2} \right\} + E_F \end{pmatrix} \begin{pmatrix} f(r) \\ g(r) \end{pmatrix} = E \begin{pmatrix} f(r) \\ g(r) \end{pmatrix} \quad (8)$$

for $f(r)$ and $g(r)$ inside the QD ($r < R_o$) or QR ($R_i < r < R_o$). In Eq. (8), $n(r)$ denotes the magnetic flux (per flux quantum) enclosed inside a disk of radius r , that is, $n(r) = n_\Phi/2$ for setups (i) and (ii) and $n(r) = Br^2\pi/\Phi_0$

for QDs and QRs, respectively.

Moreover, we consider three different setups for the magnetic field: (i) no magnetic field, (ii) no magnetic field inside a superconductor QR, but with a magnetic flux $\Phi = \pi R_i^2 B$ enclosed by the QR, where the flux quantization of a superconductor requires $2\Phi/\Phi_0 \in \mathbb{Z}$ with the magnetic flux quantum $\Phi_0 = 2\pi\hbar/e$, and (iii) a constant magnetic field $\mathbf{B} = B\mathbf{e}_z$ spread over the entire xy plane and penetrating into the QR. For setups (i) and (ii), $n_\Phi = 2\Phi/\Phi_0 \in \mathbb{Z}$ and we choose the gauge $\mathbf{A}(\mathbf{r}) = (\Phi/2\pi r)\mathbf{e}_\theta$, where \mathbf{e}_θ is the unit vector associated with the angular coordinate θ and Φ the flux enclosed by R_i [that is, $\Phi = 0$ in setup (i) and $\Phi = BR_i^2\pi$ in setup (ii)]. On the other hand, for setup (iii) we choose $\mathbf{A}(\mathbf{r}) = (Br/2)\mathbf{e}_\theta$ and $n_\Phi = [2\Phi/\Phi_0]$ denotes the integer closest to $2\Phi/\Phi_0$, where $\Phi = \pi R_i^2 B$ is the magnetic flux enclosed by $r < R_i$ in a QR, while in the case of a QD $n_\Phi = 0$.

First, we note that for setups (i)-(iii) and a radially symmetric confinement $V(r)$ the commutator $[\hat{H}, \hat{L}_{\text{eff}}] = 0$, where

$$\hat{L}_{\text{eff}} = \hat{L}_z + \frac{\hbar(1+n_\Phi)}{2}\tau_z \quad (6)$$

is an effective angular momentum operator, \hat{L}_z the angular momentum operator in z direction, and τ_z the respective Pauli matrix in particle-hole space. Thus, the eigenstates of the BdG Hamiltonian (1) can be written as

$$\Psi(r) = \begin{pmatrix} u(\mathbf{r}) \\ v(\mathbf{r}) \end{pmatrix} = \frac{1}{\sqrt{2\pi}} \begin{pmatrix} e^{im\theta} e^{i\varphi_\alpha/2} f(r) \\ e^{i(m+1+n_\Phi)\theta} e^{-i\varphi_\alpha/2} g(r) \end{pmatrix}, \quad (7)$$

where φ_α is the phase of $\alpha = |\alpha|e^{i\varphi_\alpha}$ and m is the angular momentum of the electronic component, which we use as a quantum number to label the eigenstates.

Inserting this ansatz into the BdG equation leads to the radial equation

for setup (iii). If energies and lengths are measured in terms of the Fermi energy E_F and the Fermi wavelength $\lambda_F = 2\pi\hbar/\sqrt{2m^*|E_F|}$, the solutions depend only on R_o ,

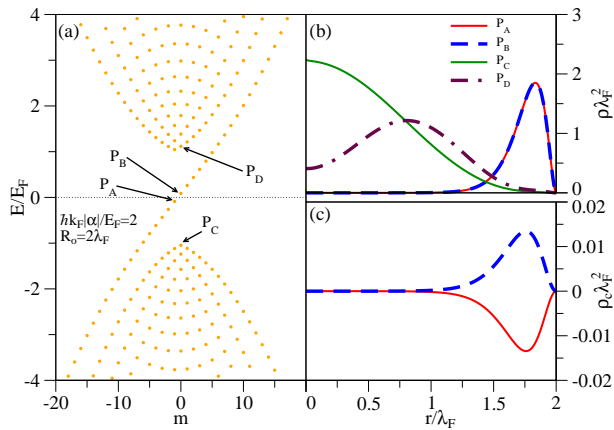


FIG. 3. (Color online) (a) Calculated excitation spectrum as well as (b) probability and (c) charge densities, $\rho(r) = |f(r)|^2 + |g(r)|^2$ and $\rho_c(r) = |f(r)|^2 - |g(r)|^2$, respectively, for selected excitations in a QD with radius $R_o = 2\lambda_F$ and pairing parameter $p = 2$. Here, the states shown in panels (b) and (c) are marked in the energy spectrum, panel (a). The charge densities of modes P_C and P_D are not displayed in panel (c) because their charge densities are two orders of magnitude larger than those of P_A and P_B .

R_i , B , and the effective pairing parameter

$$p = \frac{\hbar k_F |\alpha|}{E_F}, \quad (9)$$

where the Fermi wavevector is given by $k_F = 2\pi/\lambda_F$. In all three setups, the BdG Hamiltonian (1) exhibits particle-hole symmetry, that is, for each mode with energy E there is another mode with energy $-E$. Consequently, for a given magnetic field or flux Φ the excitation energy denoted by the quantum number m , $E_m(\Phi)$, satisfies the relation $E_m(\Phi) = -E_{-(m+1+n_\Phi)}(\Phi)$.

To solve Eq. (8) and obtain the excitation spectrum and eigenstates, we employ a finite difference scheme. However, as detailed in Appendix A, we can also obtain the solutions for the setups (i) and (ii) analytically.

III. SPECTRAL AND CHARGE PROPERTIES OF QUANTUM DOTS AND QUANTUM RINGS

A. No magnetic flux

First, we investigate the situations of QDs and QRs where no magnetic field is present (see Fig. 2), that is, case (i) where $n_\Phi = 0$ and $n(r) = 0$ in Eq. (8). Figures 3 and 4 show the excitation spectra as well as the amplitudes and charge densities of selected excitations for a QD and a QR in the topological regime ($E_F > 0$) with the pairing parameter $p = 2$. The radius of the QD is chosen to be $R_o = 2\lambda_F$, while the inner and outer radii of the QR are chosen as $R_i = 0.2\lambda_F$ and $R_o = 2\lambda_F$, respectively.

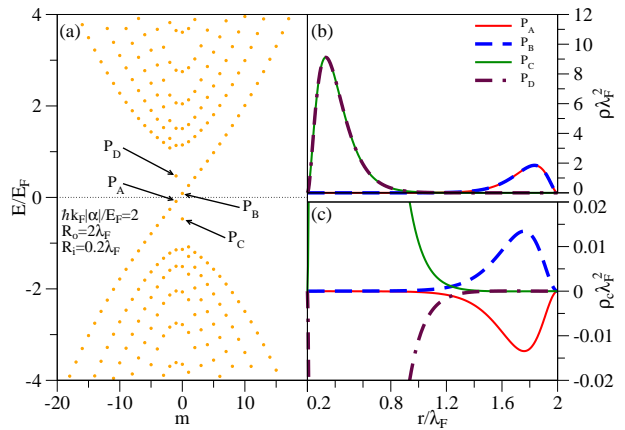


FIG. 4. (Color online) (a) Calculated excitation spectrum as well as (b) probability and (c) charge densities, $\rho(r) = |f(r)|^2 + |g(r)|^2$ and $\rho_c(r) = |f(r)|^2 - |g(r)|^2$, respectively, for selected excitations in a QR with outer radius $R_o = 2\lambda_F$, inner radius $R_i = 0.2\lambda_F$, and pairing parameter $p = 2$. Here, the states shown in panels (b) and (c) are marked in the energy spectrum, panel (a).

In Fig. 3 (a), one can see that there is a gap in the excitation spectrum of the QD with the amplitudes of selected excitations (P_C , P_D) outside the gap shown in Fig. 3 (b). As expected in the topological regime, however, there are also modes inside the gap (P_A , P_B), which correspond to charged modes localized at the edge of the QD [see Figs. 3 (b) and (c)]. A QR as illustrated in Fig. 4 possesses similar characteristics, that is, edge modes inside the superconducting gap (P_A , P_B), but now with additional charged modes (such as the modes P_C and P_D in Fig. 4) localized at the inner edge—at least as long as the spatial extent of the edge modes (essentially controlled by the parameter p for small energies E , see also Sec. III B below as well as Appendix A) is small enough to prevent significant overlap between states localized at opposite edges.

However, in neither case, QD or QR, is there a mode with exactly zero energy (see below). Moreover, the energy spectrum in Fig. 4 (a) illustrates that the slope of the inner edge modes is steeper than the slope of the outer edge modes. This can be qualitatively understood as a consequence of the conservation of the operator \hat{L}_{eff} , which in turn requires eigenstates associated with a fixed electronic angular momentum quantum number m to possess a higher group velocity if they are localized at the inner edge ($r \approx R_i$) than if they are localized at the outer edge ($r \approx R_o$).

Figure 5 shows how the energy spectrum of a QR with $p = 2$ and an outer radius of $R_o = 10\lambda_F$ depends on the inner radius R_i . For comparison, we also show the energy spectrum of a QD with the same parameters as the QR. As R_i increases, there are two features that can be seen in Fig. 5: First, the absolute value of the slope of the inner edge modes decreases with increasing R_i , which can again be explained as originating from the conservation of

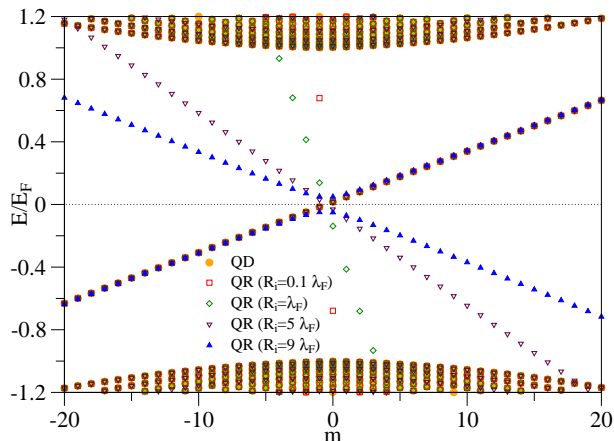


FIG. 5. (Color online) (a) Calculated excitation spectra for excitations in a QD and QRs with outer radius $R_o = 10\lambda_F$, different inner radii R_i , and pairing parameter $p = 2$.

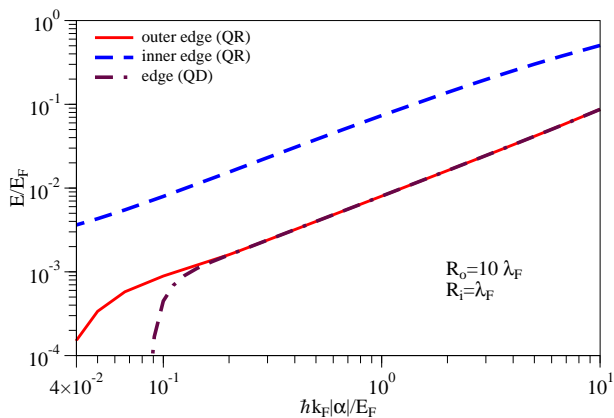


FIG. 6. (Color online) Dependence of the lowest energies of the edge modes in a QD with radius $R_o = 10\lambda_F$ as well as of the inner and outer edge modes in a QR with radii $R_o = 10\lambda_F$ and $R_i = \lambda_F$ as a function of the pairing parameter p .

the operator \hat{L}_{eff} and the resulting requirement that the group velocity should decrease as the radius increases. Second, the width $R_o - R_i$ of the QR decreases with increasing R_i and eventually the edge modes from the inner and outer edge modes overlap, which leads to the opening up of a hybridization gap as illustrated by the case of $R_i = 9\lambda_F$ in Fig. 5.

Next, we investigate the dependence of the lowest energy of the edge modes on the pairing parameter p , Eq. (9), for QDs as well as for QRs. As illustrated by Fig. 6, for large values of p the lowest energy of the modes localized at the outer edge can be fitted to $E/E_F \approx 8.5 \times 10^{-3}p$ for both a QD and a QR. This agrees reasonably well to

$$\frac{E}{E_F} = \frac{p}{4\pi(R_{o/i}/\lambda_F)}, \quad (10)$$

as also found in Ref. 4 and which yields $E/E_F \approx 8.0 \times 10^{-3}p$ for $R_o = 10\lambda_F$. Likewise, the lowest energy of

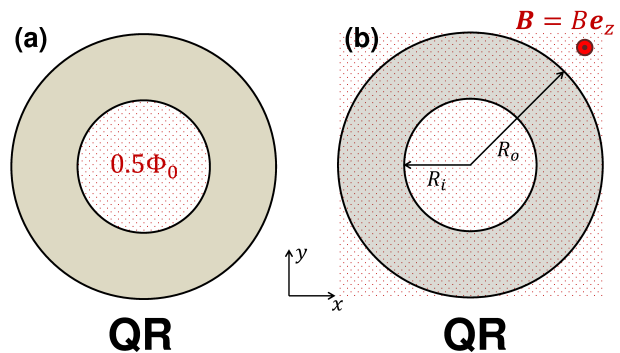


FIG. 7. (Color online) QRs as considered in Secs. III B and III C: (a) with an enclosed magnetic flux and no magnetic field penetrating into the QR and (b) a constant magnetic field. The shaded areas are areas with p -wave superconductivity.

the modes localized at the inner edge of a QR can be fitted to $E/E_F \approx 7.0 \times 10^{-2}p$, while Eq. (10) yields $E/E_F \approx 8.0 \times 10^{-2}p$ for $R_i = \lambda_F$. The deviations from the behavior described by the approximation (10) can be ascribed to the fact that in deriving this approximation curvature terms, that is, the kinetic terms in the diagonal elements of Eq. (8), have been neglected. For small values of p , curvature terms become even more important and the decrease of the lowest energy of the outer edge modes with decreasing p is more pronounced. However, the energy is never exactly zero even for very small values of p . This situation, on the other hand, can change if a magnetic flux is induced in the QR, which will be discussed in the following section.

B. Magnetic flux with no field penetration into the superconducting region

In this and the following section, we study cases (ii) and (iii), that is, the effects of a perpendicular magnetic field on a QR as shown in Fig. 7. First, we look at situation (ii), where the magnetic field is completely expelled from the QR and just induces a magnetic flux enclosed by R_i as shown in Fig. 7 (a). As mentioned above, flux quantization in this case requires the flux to be $\Phi = n_\Phi \Phi_0/2$, where n_Φ is an integer. If n_Φ is even, the results for QRs from the previous section are recovered, but with the magnetic flux shifting states and energies denoted by the electronic angular momentum quantum number m at zero flux to states denoted by $m - n_\Phi/2$, that is, $E_m(\Phi) = E_{m+n_\Phi/2}(0)$ [see also Eq. (A1) in Appendix A].

While an even integer multiple of $\Phi_0/2$ thus essentially reduces the problem to the situation of zero magnetic flux, the situation is different for an odd integer multiple of $\Phi_0/2$. Without loss of generality we can choose $\Phi = \Phi_0/2$ in that case because every other odd integer multiple of $\Phi_0/2$ can be mapped to this flux, similar to how an even integer flux can be mapped to the situation

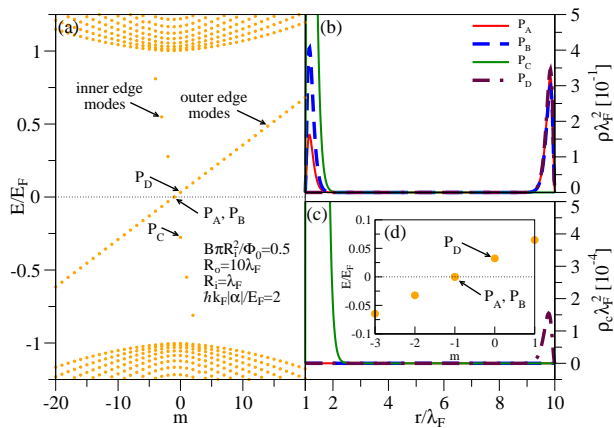


FIG. 8. (Color online) (a) Calculated excitation spectrum as well as (b) probability and (c) charge densities, $\rho(r) = |f(r)|^2 + |g(r)|^2$ and $\rho_c(r) = |f(r)|^2 - |g(r)|^2$, respectively, for selected excitations in a QR with outer radius $R_o = 10\lambda_F$, inner radius $R_i = \lambda_F$, and pairing parameter $p = 2$ if a magnetic flux of $\Phi_0/2$ is enclosed by R_i with no magnetic field penetrating into the QR. Here, the states shown in panels (b) and (c) are marked in the energy spectrum, panel (a). The amplitude of P_D in panel (b) is nearly completely overlapping with the two modes P_A and P_B at the outer radius. Panel (d) displays the excitation energies close to zero.

of zero flux.

Figure 8 displays the situation for a QR in the topological regime ($E_F > 0$) if a magnetic flux of $\Phi_0/2$ is enclosed inside the QR and no magnetic field penetrates into the superconducting region. Here, we use the radii $R_i = \lambda_F$ and $R_o = 10\lambda_F$ and the parameter $p = 2$. Similar to the situation of zero flux, there are modes with energies inside the superconducting gap and localized at the boundaries of the QR (such as P_C , P_D). In contrast to the situation of zero flux, however, there are now also two degenerate edge modes (labeled as P_A , P_B) at zero energy [see the inset Fig. 8 (d) and also Refs. 4 and 91] which are also chargeless and thus Majorana modes. This degeneracy at zero energy is a consequence of particle-hole symmetry, which for each mode with energy E requires the existence of another mode with energy $-E$.

It is important to note, however, that if there is a finite overlap between the wave functions localized at the inner and outer radii, these degenerate Majorana modes are split similar to Fig. 5 in Sec. III A. This overlap is affected in two ways, namely by the width $R_o - R_i$ of the ring and by the spatial extent of the edge states.

The effect of a narrow width $R_o - R_i$ is illustrated in Fig. 9, where we use a QR with the pairing parameter $p = 2$, the flux $\Phi = \Phi_0/2$, and the inner and outer radii of $R_i = 9\lambda_F$ and $R_o = 10\lambda_F$, respectively. Here, the finite overlap between the two particle-hole symmetric modes P_A and P_B leads to a noticeable splitting between them of $E_{A/B} \approx \pm 0.05E_F$. This is due to a large overlap between the edge modes at the inner and the outer boundaries, which also results in a finite charge density of P_A and

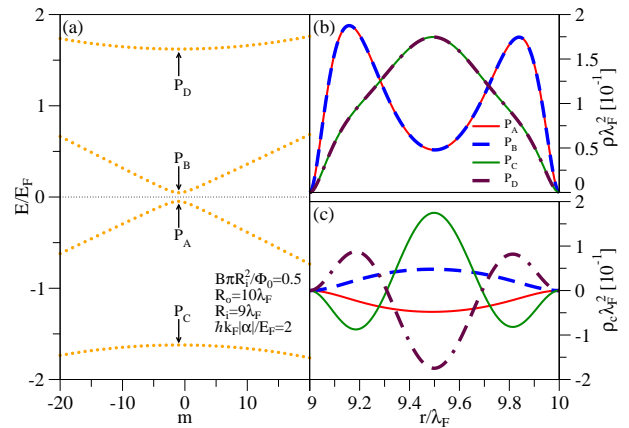


FIG. 9. (Color online) (a) Calculated excitation spectrum as well as (b) probability and (c) charge densities, $\rho(r) = |f(r)|^2 + |g(r)|^2$ and $\rho_c(r) = |f(r)|^2 - |g(r)|^2$, respectively, for selected excitations in a QR with outer radius $R_o = 10\lambda_F$, inner radius $R_i = 9\lambda_F$, and pairing parameter $p = 2$ if a magnetic flux of $\Phi_0/2$ is enclosed by R_i with no magnetic field penetrating into the QR. Here, the states shown in panels (b) and (c) are marked in the energy spectrum, panel (a).

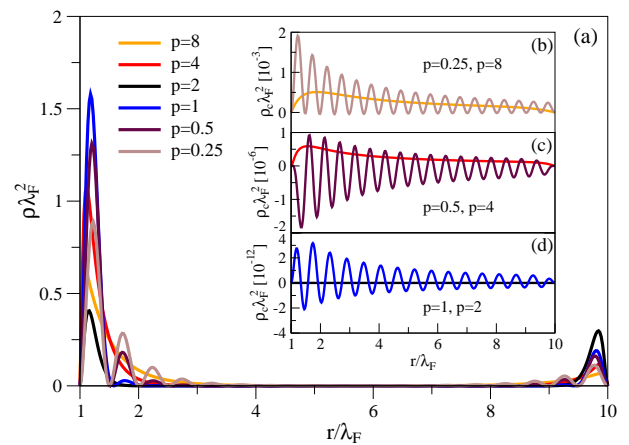


FIG. 10. (Color online) (a) Calculated probability and (b)-(d) charge densities, $\rho(r) = |f(r)|^2 + |g(r)|^2$ and $\rho_c(r) = |f(r)|^2 - |g(r)|^2$, respectively, for the excitations at or close to zero energy in a QR with outer radius $R_o = 10\lambda_F$, inner radius $R_i = \lambda_F$, and different pairing parameters p if a magnetic flux of $\Phi_0/2$ is enclosed by R_i with no magnetic field penetrating into the QR. Panels (b)-(d) demonstrate that for $p = 2$ and $p = 1$ the charge density is zero or extremely small, while other values of p can lead to significantly higher charge densities.

P_B , similar to the situation in a wire geometry.^{80–82,85} In addition to the amplitudes and charge densities of P_A and P_B , two excitations above the superconducting gap (P_C , P_D) are also displayed.

A second parameter that affects the overlap between edge modes near zero energy is their spatial extent, which is essentially controlled by the pairing parameter p , Eq. (9), where edge modes are most localized for values in the vicinity of $p = 2$, while they become more extended

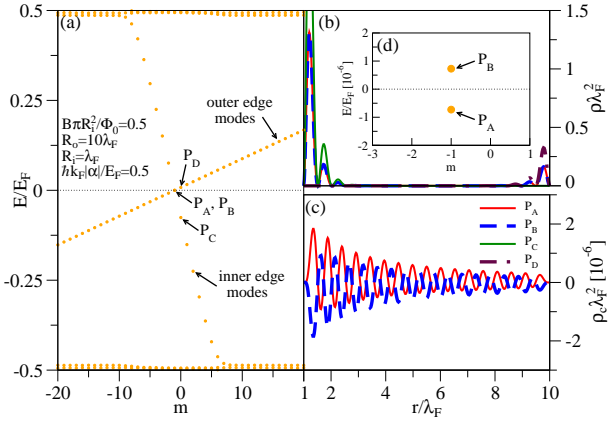


FIG. 11. (Color online) (a) Calculated excitation spectrum as well as (b) probability and (c) charge densities, $\rho(r) = |f(r)|^2 + |g(r)|^2$ and $\rho_c(r) = |f(r)|^2 - |g(r)|^2$, respectively, for selected excitations in a QR with outer radius $R_o = 10\lambda_F$, inner radius $R_i = \lambda_F$, and pairing parameter $p = 0.5$ if a magnetic flux of $\Phi_0/2$ is enclosed by R_i with no magnetic field penetrating into the QR. Here, the states shown in panels (b) and (c) are marked in the energy spectrum, panel (a). The charge densities of modes P_C and P_D are not displayed in panel (c) because their charge densities are four orders of magnitude larger than those of P_A and P_B . Panel (d) displays the excitation energies close to zero.

if p is decreased or increased [see Fig. 10 (a)]. Likewise, Fig. 10 (d) illustrates that close to $p = 2$, where the charge density even vanishes and the excitation energy is zero, the charge density is very small as, for example, in the case of $p = 1$. In Figs. 10 (b) and (c), on the other hand, the charge density increases by several orders of magnitude for values of p farther away from $p = 2$.⁹⁶

Moreover, Fig. 10 shows that for $p < 2$ the probability and charge densities exhibit oscillations, while there is no oscillatory behavior for $p \geq 2$. This behavior can be understood by looking at the form of the wave functions given by Eqs. (A3) and (A4) in Appendix A: The wave functions (A3) consist only of Bessel and Neumann functions, whose arguments are purely imaginary for $p \geq 2$ and energies close to zero and thus result in non-oscillatory wave functions. For $p < 2$, on the other hand, the arguments of the Bessel and Neumann functions are not purely imaginary for energies close to zero, which leads to oscillating wave functions.

To corroborate this statement, Fig. 11 shows the excitation spectrum, several amplitudes, and several charge densities of the same QR as in Fig. 8, but with $p = 0.5$. While in Fig. 8 we obtain two Majorana-bound states P_A and P_B as degenerate chargeless modes at exactly zero energy within the numerical accuracy of our calculation, there is a finite overlap between the two corresponding states P_A and P_B in Fig. 11, which leads to a small, but finite splitting with $E_{A/B} \approx \pm 10^{-8} E_F$. Likewise, the charge carried by the particle-hole symmetric modes P_A and P_B in Fig. 11 (c) is very small, but finite and spread over the entire ring [see also Figs. 10 (b)-(d)], similar to

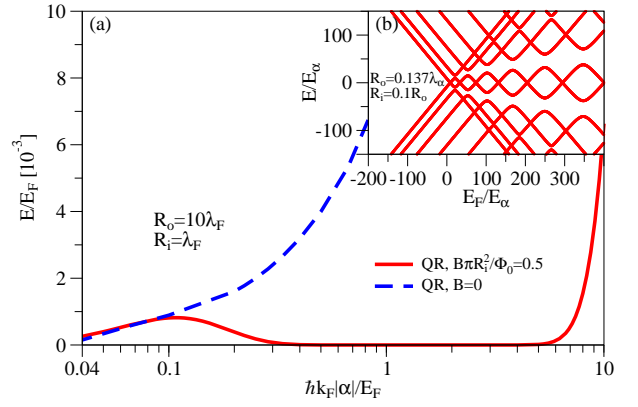


FIG. 12. (Color online) (a) Dependence of the lowest energies of the (outer) edge modes in a QR with radii $R_o = 10\lambda_F$ and $R_i = \lambda_F$ as a function of the pairing parameter p if no magnetic flux or a magnetic flux of $\Phi_0/2$ is enclosed by R_i with no magnetic field penetrating into the QR. The inset (b) shows the dependence of the energy spectrum at $m = -1$ on the Fermi energy for a QR which is threaded by a magnetic flux of $\Phi_0/2$. In the inset (b), energies are measured in units of $E_\alpha = m^*|\alpha|^2$ and lengths in units of $\lambda_\alpha = 2\pi\hbar/m^*|\alpha|$.

the situation found in Ref. 85 for one-dimensional topological superconductor wires.⁹⁷

In this sense, one can thus speak of the modes P_A and P_B in Fig. 11 as being Majorana-bound states only approximately. The difference between these modes and the remaining ordinary chiral edge modes away from zero energy can be revealed by their charge densities: While the charge density of those approximate Majorana-bound states is spread over the entire QR and very small as displayed in Figs. 10 (b)-(d) and 11 (c), the charge density of chiral edge modes away from zero energy, such as P_C and P_D in Fig. 8 (c), is localized at the edges and typically several orders of magnitude larger.

The dependence of the lowest energy of the edge modes on the pairing parameter p is displayed in Fig. 12 (a) for a QR with radii $R_o = 10\lambda_F$ and $R_i = \lambda_F$ and a magnetic flux of $\Phi_0/2$. For comparison, the p dependence in the case of zero flux is also included. While in the absence of any magnetic flux the energy increases monotonously as discussed in Fig. 6 in Sec. III A, the situation is different in the presence of a half-integer flux. Here, there is a region where the energy is very small and extremely close to zero, such as the situations depicted in Figs. 8 and 11. As the value of p is increased or decreased, for example, by changing the p -wave pairing α accordingly, the edge modes become more extended leading to a finite overlap and an increase in the splitting between the two particle-hole symmetric modes close to zero energy.

Figure 12 (b) shows the dependence of the energy spectrum at $m = -1$ on the Fermi energy of a QR threaded by a magnetic flux of $\Phi_0/2$ for a fixed α . One can clearly see the transition between the topologically trivial regime for $E_F < 0$, where no edge modes with energies inside the bulk gap are present, and the topological regime,

where such states arise. Moreover, those low-energy edge modes exhibit oscillations where the zeros are associated with jumps in the parity of the superconducting ground state.^{81,82,85} At these points, exact Majorana modes with zero energy and charge as in Fig. 8 can be found, while energies away from zero correspond to approximate Majorana modes like in Fig. 11. With increasing distance $R_o - R_i$, the amplitude of these oscillations decreases as the overlap between edge modes situated at opposite edges decreases.

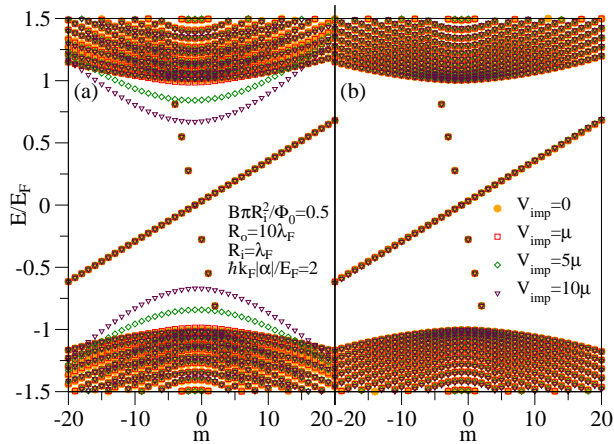


FIG. 13. (Color online) Calculated excitation spectra in a QR with outer radius $R_o = 10\lambda_F$, inner radius $R_i = \lambda_F$, and pairing parameter $p = 2$ if a magnetic flux of $\Phi_0/2$ is enclosed by R_i with no magnetic field penetrating into the QR and a concentric ring of an array of nonmagnetic impurities, characterized by the impurity potential V_{imp} . The impurities are situated at $r = (R_o - R_i)/2$ in panel (a) and at $r = 0.9775R_o$ in panel (b).

Finally, using a very simple model, we can compare the effects of impurities on the edge and bulk modes. We consider a concentric ring of an array of nonmagnetic impurities characterized by the impurity potential V_{imp} . Figure 13 (a) shows the excitation spectrum for a QR with radii $R_o = 10\lambda_F$ and $R_i = \lambda_F$, a magnetic flux of $\Phi_0/2$, and different strengths of V_{imp} for impurities situated at $r = (R_o - R_i)/2$. Since the impurities are far away from the edges, the edge modes are not affected by the impurity potential, whereas the modifications of the bulk modes are clearly visible. On the other hand, if the impurities are situated at an edge, as is the case in Fig. 13 (b), both the bulk and edge modes are not significantly changed. Thus, in contrast to bulk modes the edge modes are not substantially affected by nonmagnetic impurities, regardless of the position of the impurities. This striking difference between the role of perturbations on the edge and bulk states in Fig. 13 is consistent with the robustness that we can associate with the Majorana-like states.

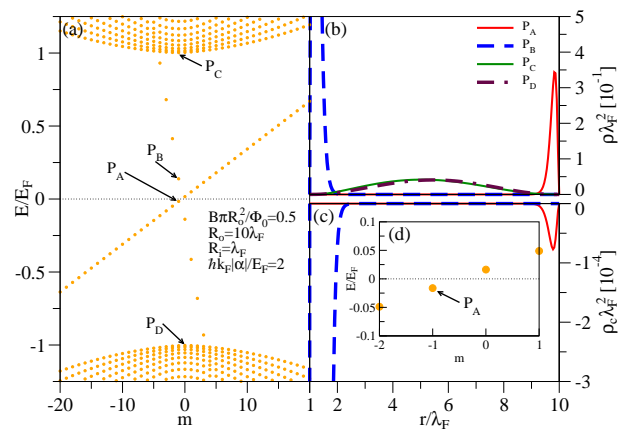


FIG. 14. (Color online) (a) Calculated excitation spectrum as well as (b) probability and (c) charge densities, $\rho(r) = |f(r)|^2 + |g(r)|^2$ and $\rho_c(r) = |f(r)|^2 - |g(r)|^2$, respectively, for selected excitations in a QR with outer radius $R_o = 10\lambda_F$, inner radius $R_i = \lambda_F$, and pairing parameter $p = 2$ if a constant magnetic field penetrates into the QR with R_o enclosing a magnetic flux of $\Phi_0/2$. Here, the states shown in panels (b) and (c) are marked in the energy spectrum, panel (a). Panel (d) displays the excitation energies close to zero.

C. Magnetic field penetrating into the superconducting region

In the preceding discussions it has always been assumed that the magnetic field cannot penetrate into the superconducting region. Finally, we now also investigate the situation shown in Fig. 7 (b), where the perpendicular magnetic field can penetrate into the QR, that is, case (iii).

Our motivation for investigating this model is twofold: As already mentioned, if the chiral p -wave BdG Hamiltonian in Eq. (1) is regarded as a simplified toy model for other, more complex hybrid structures with only proximity-induced pairing, a magnetic field can exist in these systems without being expelled like in a usual superconductor. On the other hand, if the system investigated is an extended three-dimensional superconductor, a magnetic field cannot penetrate far into this superconducting material and decays within the London penetration depth.^{98,99} However, if the sample is a thin film, that is, a film with a thickness smaller than the London penetration depth and a large extent of the base area, an applied in-plane magnetic field can be very accurately described as a constant field inside the film.¹⁰⁰ Here, we make the simplifying assumption that such a behavior could also be applicable for an out-of-plane magnetic field.

Figure 14 depicts a situation where a constant magnetic field B spread over the entire xy plane and corresponding to a magnetic flux $\pi R_o^2 B = 0.5\Phi_0$ enclosed by the outer radius R_o is applied and thus induces no additional phase dependence of the p -wave pairing amplitude in Eq. (1), $n_\Phi = 0$. The remaining parameters are chosen

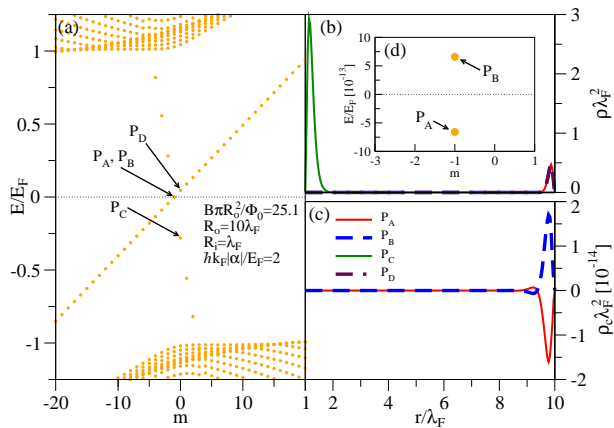


FIG. 15. (Color online) (a) Calculated excitation spectrum as well as (b) probability and (c) charge densities, $\rho(r) = |f(r)|^2 + |g(r)|^2$ and $\rho_c(r) = |f(r)|^2 - |g(r)|^2$, respectively, for selected excitations in a QR with outer radius $R_o = 10\lambda_F$, inner radius $R_i = \lambda_F$, and pairing parameter $p = 2$ if a constant magnetic field penetrates into the QR with R_o enclosing a magnetic flux of $25.1\Phi_0$. Here, the states shown in panels (b) and (c) are marked in the energy spectrum, panel (a). The amplitude of P_D in panel (b) is nearly completely overlapping with the two modes P_A and P_B . The charge densities of modes P_C and P_D are not displayed in panel (c) because their charge densities are 14 orders of magnitude larger than those of P_A and P_B . Panel (d) displays the excitation energies close to zero.

as $p = 2$, $R_o = 10\lambda_F$, and $R_i = \lambda_F$. Analyzing this setup, we can see that the behavior is very similar to the situation with zero flux, that is, there are edge modes with finite energies, but none with zero energy.

Next, we increase the strength of the magnetic field to a value corresponding to the magnetic flux $\pi R_o^2 B = 25.1\Phi_0$, while keeping the remaining parameters p , R_i , and R_o the same. For this strength of the magnetic field, an additional phase $-n_\Phi\theta$ with $n_\Phi = 1$ is induced in the p -wave pairing amplitude, just like in case (ii) with a half-integer flux enclosed by R_i , in which case Majorana modes—or more strictly speaking at least Majorana-like modes very close to zero energy and with tiny charge densities—were possible. Figure 15 illustrates that this is also the case here: The two particle-hole symmetric modes P_A and P_B display a finite splitting of $E_{A/B} \approx \pm 7 \times 10^{-13} E_F$ with extremely small, but finite charge densities, although in this case the charge densities are not spread over the QR, but localized at the edges [see Fig. 15 (c)].

In this sense, Majorana-like modes (which originate from inducing a phase $-\theta$ in the p -wave pairing) persist even if magnetic fields penetrate into the superconducting region. For comparison, edge modes away from zero energy (P_C , P_D) are also shown in Fig. 15. While the amplitude of the outer edge mode P_D in Fig. 15 (b) is nearly completely overlapping with the two Majorana-like modes P_A and P_B , its charge density is 14 orders of magnitudes larger. Moreover, the energy spectrum out-

side the superconducting gap in Fig. 15 (a) reflects the increasing importance of orbital effects as the strength of the magnetic field inside the superconducting ring increases.

IV. EXPERIMENT

First, we briefly discuss possible systems in which the phenomena described above can be observed and which might be more readily available than intrinsic p -wave superconductor materials. Following several proposals,^{23–26} a possible implementation of effective p -wave pairing can be in a semiconductor ring with strong Rashba spin-orbit coupling^{27,28} that is brought into close proximity to an s -wave superconductor ring, which induces superconductivity into the semiconductor and which can be threaded by a magnetic flux $n_\Phi\Phi_0/2$. Flux quantization in a superconductor ring requires n_Φ to be an integer. Additionally, a Zeeman term is needed to break time-reversal symmetry and drive the induced p -wave superconductor into the topologically nontrivial phase.¹⁰¹ To engineer this, a ferromagnet is placed in the vicinity of the semiconductor ring. The ferromagnet then induces a Zeeman term E_Z into the semiconductor ring via the ferromagnetic proximity effect, while orbital terms induced by the ferromagnet can be omitted. Thus, the semiconductor ring is sandwiched between two rings, one superconducting the other ferromagnetic, which induce superconductivity and ferromagnetism, respectively, in the semiconductor ring.

Then, analogous to Eq. (1), the BdG Hamiltonian for the semiconductor ring (situated in the xy -plane) in particle-hole space is given by

$$\hat{H} = \begin{pmatrix} H_0(\mathbf{r}) & \Delta(\mathbf{r}) \\ \Delta^\dagger(\mathbf{r}) & -\hat{s}_y H_0^*(\mathbf{r}) \hat{s}_y \end{pmatrix}, \quad (11)$$

where

$$H_0(\mathbf{r}) = \frac{[\hat{\mathbf{p}} + e\mathbf{A}(\mathbf{r})]^2}{2m^*} - E_F + V(r) + \alpha_{\text{SOC}} \{ \hat{\mathbf{s}} \times [\hat{\mathbf{p}} + e\mathbf{A}(\mathbf{r})] \} \cdot \mathbf{e}_z + E_Z \mathbf{n} \cdot \hat{\mathbf{s}} \quad (12)$$

and

$$\Delta(\mathbf{r}) = \Delta e^{-im_\Phi\theta} \hat{\mathbf{1}} \quad (13)$$

are now matrices in spin-1/2 space. As before, \mathbf{r} , $\hat{\mathbf{p}}$, $\mathbf{A}(\mathbf{r})$, m^* , E_F , and $V(r)$ denote the position in the xy plane, the two-dimensional momentum operator, the magnetic vector potential, the electronic effective mass, the Fermi energy, and the confinement, while α_{SOC} is the (Rashba) spin-orbit coupling strength, Δ the proximity-induced s -wave pairing amplitude,¹⁰² E_Z the proximity-induced Zeeman term, $\hat{\mathbf{s}}$ a vector containing the three Pauli matrices in spin-1/2 space (\hat{s}_x , \hat{s}_y , and \hat{s}_z) and \mathbf{n} the direction of the proximity induced magnetization.

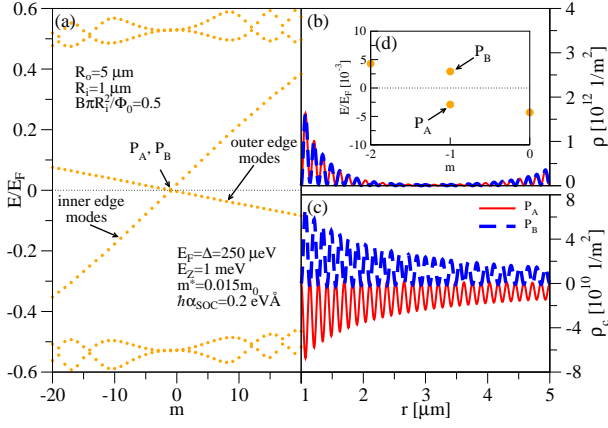


FIG. 16. (Color online) (a) Calculated excitation spectrum as well as (b) probability and (c) charge densities, $\rho(r)$ and $\rho_c(r)$, respectively, of the approximate Majorana-bound states in an InSb ring with induced pairing and ferromagnetism, outer radius $R_o = 5 \mu\text{m}$, and inner radius $R_i = 1 \mu\text{m}$. Excitation energies close to zero, including the approximate Majorana-bound states (labeled P_A and P_B) are shown in panel (d).

The system described by Eqs. (11)-(13) exhibits the same features as the model of a spinless p -wave superconductor discussed in Secs. II and III, but with the condition $|E_Z| - \sqrt{E_F^2 + |\Delta|^2} \leq 0$ separating the topological trivial ($<$) and nontrivial ($>$) regimes. Likewise, the conserved quantity is now given by the operator

$$\hat{J}_{\text{eff}} = \hat{L}_z + \frac{\hbar}{2}s_z + \frac{\hbar m\Phi}{2}\tau_z \quad (14)$$

instead of \hat{L}_{eff} , that is, the orbital angular momentum \hat{L}_z is replaced by the total angular momentum $\hat{L}_z + (\hbar/2)s_z$, while $n_\Phi + 1$ is replaced by n_Φ . Then, the eigenstates read as

$$\Psi(r) = \frac{1}{\sqrt{2\pi}} \begin{pmatrix} e^{im\theta} e^{i\varphi\Delta/2} a(r) \\ e^{i(m+1)\theta} e^{i\varphi\Delta/2} b(r) \\ e^{i(m+n_\Phi)\theta} e^{-i\varphi\Delta/2} c(r) \\ e^{i(m+1+n_\Phi)\theta} e^{-i\varphi\Delta/2} d(r) \end{pmatrix}, \quad (15)$$

where $\Delta = |\Delta|e^{i\varphi\Delta}$. However, the basic conclusions from Secs. II and III are valid also for this system.

As an illustration of this, Fig. 16 shows the excitation spectrum calculated from Eqs. (11)-(13) and corresponding to an InSb⁶⁶ ($m^* = 0.015m_0$, $\hbar\alpha_{\text{SOC}} = 0.2 \text{ eV}\text{\AA}$) ring with an inner radius of $R_i = 1 \mu\text{m}$ and an outer radius of $R_o = 5 \mu\text{m}$ with an induced s -wave pairing amplitude of $\Delta = 250 \mu\text{eV}$, an induced Zeeman splitting of $E_Z = 1 \text{ meV}$ in z -direction ($\mathbf{n} = \mathbf{e}_z$), and a Fermi energy of $E_F = 250 \mu\text{eV}$. Moreover, a magnetic flux of $\Phi = \Phi_0/2$ is enclosed by the rings without a magnetic field penetrating into the semiconductor, that is, we are looking at case (ii) from Secs. II and III with $n_\Phi = 1$ and $\mathbf{A}(\mathbf{r}) = (\Phi/2\pi r)\mathbf{e}_\theta = (\Phi_0/4\pi r)\mathbf{e}_\theta$.

For convenience and for the sake of easy comparison to the previous sections, we use the angular momentum

m of the electronic spin up component, that is, the first component in Eq. (15) to label the modes. Exactly as in the case of Fig. 11, there are edge modes localized at the inner and outer radii as expected in the topological regime and two approximate Majorana-bound states P_A and P_B close to zero energy (with a splitting of $E_{A/B} \approx \pm 7.3 \times 10^{-7} \text{ eV} \approx \pm 2.9 \times 10^{-3} E_F$) and with amplitudes and charge densities similar to those in Fig. 11, as expected for a magnetic flux of $\Phi = \Phi_0/2$.¹⁰³

Following the proposal in Ref. 85 for a wire, where the situation is very similar, one possible way to experimentally detect the presence of Majorana modes in a QR could be by charge sensing: As shown in Secs. III B, the two Majorana-bound states are split into two particle-hole symmetric modes with very small, but finite energies if their wave functions localized at the inner and outer boundaries of the ring have a finite overlap. Likewise, those excitations possess a small, but finite charge density which is spread over the entire (radial extent of) the ring. This behavior is different from the other Andreev-bound states/chiral edge modes away from zero energy whose charge distribution is localized at a given edge. The charge distribution of a given mode at different points in the QR can then be probed by single-electron transistors acting as charge detectors.⁸⁵ In Appendix B, we directly show the similarity of Majorana-like states in a one-dimensional finite wire and a QR with cylindrical geometry.

Most proposals to detect Majorana modes in a condensed matter context usually involve conductance or—in the case of rings—interference measurements.^{62,63,66,95} The signature of Majorana modes in these measurements is typically a zero-bias conductance peak or conductance peaks close to zero. However, these zero-bias conductance peaks can also originate from phenomena other than Majorana modes (such as the Kondo effect⁷³), which in turn makes it difficult to identify Majorana modes conclusively. Combining these conductance measurements with charge measurements as mentioned above could, on the other hand, then be used to identify the (approximate) Majorana modes.⁸⁵ This is because the charge distribution of split Majorana modes is spread over the entire ring, whereas phenomena such as the Kondo effect are restricted to the boundaries and possible changes in the charge density could only be detected there.

V. CONCLUSIONS

We have theoretically studied chiral p -wave superconductivity in QDs and QRs and calculated the quasiparticle excitation spectra in these structures as well as the corresponding excitation amplitudes and charge densities. In the topological regime, we can observe the chiral edge modes localized at the boundaries and possessing finite energy in QDs and QRs, whereas no edge modes appear in the topologically trivial regime. However, none

of the edge modes in the topological regime possess zero energy, that is, none of them is a Majorana mode. Only by applying a magnetic field which is expelled from the QR, but which creates a flux that is an odd integer multiple of $\Phi_0/2 = \pi\hbar/e$, Majorana modes, that is, degenerate edge modes with zero energy and zero charge density, become possible in a QR in the topological regime, whereas none can be found in a QDs. Finite-size effects result in a splitting of these degenerate edge modes, leading to approximate Majorana modes in the sense that they have only approximately zero energy and zero charge density and are only approximately degenerate. This small, but finite charge distribution is then spread over the entire QR which allows for charge sensing measurements—in conjunction with other measurements at the edges—to probe the presence of Majorana modes. In the case of a magnetic field penetrating into the superconducting region, edge modes with approximately zero energy and charge can still be supported, although in this case the charge distribution is not necessarily spread over the en-

tire QR.

ACKNOWLEDGMENTS

We are grateful to İnanç Adagideli and Baris Pekerten for many discussions which were directly motivating this work. We thank Jong Han, Alex Matos-Abiague, and John Wei for stimulating discussions and suggestions. This work was supported by U.S. ONR Grant No. N000141310754 and DFG Grant No. SCHA 1899/1-1 (B.S.) as well as U.S. DOE, Office of Science BES, under Award de-sc0004890 (I.Ž.).

Appendix A: Analytical solution

For setups (i) and (ii), Eq. (8) reduces to

$$\begin{pmatrix} -\frac{\hbar^2}{2m^*} \left[\partial_r^2 + \frac{1}{r} \partial_r - \frac{(m+n_\Phi/2)^2}{r^2} \right] - E_F & -\hbar|\alpha| \left(\partial_r + \frac{m+1+n_\Phi/2}{r} \right) \\ -\hbar|\alpha| \left(\partial_r - \frac{m+n_\Phi/2}{r} \right) & \frac{\hbar^2}{2m^*} \left[\partial_r^2 + \frac{1}{r} \partial_r - \frac{(m+1+n_\Phi/2)^2}{r^2} \right] + E_F \end{pmatrix} \begin{pmatrix} f(r) \\ g(r) \end{pmatrix} = E \begin{pmatrix} f(r) \\ g(r) \end{pmatrix}, \quad (\text{A1})$$

where $m + n_\Phi/2$ is either an integer or a half-integer. We note that in the presence of a magnetic flux which is an integer multiple of Φ_0 , that is, in the case of n_Φ being an even integer, the energies E and functions $f(r)$ and $g(r)$ for a fixed electronic angular momentum quantum number m in Eq. (A1) are determined by the same equation as the energies and functions for zero magnetic flux, but with an angular momentum quantum number $m + n_\Phi/2$. Thus, if n_Φ is an even integer, the energies and states with the angular momentum quantum number m are the same as the energies and states with the angular momentum quantum number $m + n_\Phi/2$ at zero flux, that is, $E_m(\Phi) = E_{m+n_\Phi/2}(0)$.

After those remarks on the special case in which n_Φ is an even integer we now turn our attention to solving Eq. (A1) for any integer n_Φ . As mentioned in Sec. II, the excitation energies $E_m(\Phi)$ satisfy the relation $E_m(\Phi) = -E_{-(m+1+n_\Phi)}(\Phi)$ due to particle-hole symmetry.

A solution to Eq. (A1) can be obtained analytically because the diagonal components of the matrix correspond to Bessel's equation, while the off-diagonal elements correspond to raising and lowering operators for Bessel functions.¹⁰⁴ A general solution to Eq. (A1) at energy E thus reads

$$\begin{pmatrix} f(r) \\ g(r) \end{pmatrix} = a\eta_+(r) + b\eta_-(r) + c\chi_+(r) + d\chi_-(r) \quad (\text{A2})$$

with the four fundamental solutions

$$\eta_\pm(r) = \begin{pmatrix} u_\pm J_l(\kappa_\pm r) \\ v_\pm J_{l+1}(\kappa_\pm r) \end{pmatrix}, \quad \chi_\pm(r) = \begin{pmatrix} u_\pm Y_l(\kappa_\pm r) \\ v_\pm Y_{l+1}(\kappa_\pm r) \end{pmatrix}, \quad (\text{A3})$$

where $J_l(x)$ and $Y_l(x)$ are the Bessel and Neumann functions, $l = m + n_\Phi/2$ an integer or half-integer,

$$\begin{aligned} \kappa_\pm = \kappa_\pm(E) = & \frac{\sqrt{2m^*}}{\hbar} \left[E_F - m^*|\alpha|^2 \right. \\ & \left. \pm \sqrt{(E_F - m^*|\alpha|^2)^2 - E_F^2 + E^2} \right]^{1/2}, \end{aligned} \quad (\text{A4})$$

and, if $\alpha \neq 0$,

$$\begin{aligned} u_\pm = & \frac{\hbar|\alpha|\kappa_\pm}{\sqrt{\hbar^2|\alpha|^2\kappa_\pm^2 + \left(\frac{\hbar^2\kappa_\pm^2}{2m^*} - E_F - E\right)^2}} \\ v_\pm = & \frac{\frac{\hbar^2\kappa_\pm^2}{2m^*} - E_F - E}{\sqrt{\hbar^2|\alpha|^2\kappa_\pm^2 + \left(\frac{\hbar^2\kappa_\pm^2}{2m^*} - E_F - E\right)^2}}. \end{aligned} \quad (\text{A5})$$

We note that the components u_\pm and v_\pm as well as κ_\pm (if measured in units of k_F) depend only on the effective pairing parameter p given by Eq. (9) and the ratio E/E_F . Thus, in the topological regime the spatial extent (with respect to λ_F) of the edge modes at low energies is primarily determined by the parameter p . Finally, the energy E and the complex coefficients a , b , c , and d have

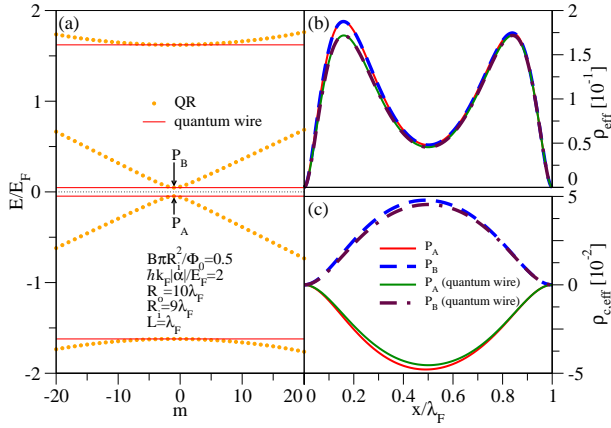


FIG. 17. (Color online) Comparison between the (a) calculated excitation spectra as well as the effective dimensionless (b) probability and (c) charge densities, $\rho_{\text{eff}}(x)$ and $\rho_{c,\text{eff}}(x)$, respectively, for selected excitations in a QR threaded by a magnetic flux of $\Phi_0/2$ and a one-dimensional wire with the same parameters. While the energy levels in the QR can be described by the quantum number m , the quantum wire has discrete energy levels. Here, the states shown in panels (b) and (c) are marked in the energy spectrum, panel (a).

to be determined from the boundary conditions for QDs and QRs.

(i) *Quantum dots.*

In the case of QDs, the boundary conditions require that $f(r)$ and $g(r)$ do not diverge at $r = 0$ and that $f(R_o) = g(R_o) = 0$. The condition at $r = 0$ can only be satisfied if $c = d = 0$ in Eq. (A2), while the condition at $r = R_o$ yields a system of two linear equations for the coefficients a and b . This system has a nontrivial solution if

$$u_+ v_- J_l(\kappa_+ R_o) J_{l+1}(\kappa_- R_o) = u_- v_+ J_l(\kappa_- R_o) J_{l+1}(\kappa_+ R_o), \quad (\text{A6})$$

which in turn represents a transcendental equation to obtain the excitation energies E for QDs.

(ii) *Quantum rings.*

For QRs, the boundary conditions $f(R_o) = g(R_o) = f(R_i) = g(R_i) = 0$ have to be satisfied. Inserting these

conditions into Eq. (A2) yields a linear system of four equations for the coefficients a , b , c , and d , which possesses a nontrivial solution if

$$\det \begin{pmatrix} \eta_+(R_o) & \eta_-(R_o) & \chi_+(R_o) & \chi_-(R_o) \\ \eta_+(R_i) & \eta_-(R_i) & \chi_+(R_i) & \chi_-(R_i) \end{pmatrix} = 0. \quad (\text{A7})$$

The excitation energies E for QRs can then be obtained from the transcendental Eq. (A7).

Appendix B: Comparison between a quantum ring and a wire

Figure 17 compares the excitation spectrum, probability and charge densities for selected excitations in a QR with outer radius $R_o = 10\lambda_F$, inner radius $R_i = 9\lambda_F$, and pairing parameter $p = 2$ if a magnetic flux of $\Phi_0/2$ is enclosed by R_i with no magnetic field penetrating into the QR and a one-dimensional wire of length $L = \lambda_F$, pairing parameter $p = 2$, and no magnetic field. The coordinate x in Figs. 17 (b) and (c) is to be read as the shifted radial coordinate $r - R_i$ in a QR and the one-dimensional coordinate l of a wire, while the effective dimensionless probability and charge densities are to be read as $\rho_{\text{eff}}(x) = \rho(r)\lambda_F^2$ and $\rho_{c,\text{eff}}(x) = \rho_c(r)\lambda_F^2$ for the QR and as $\rho_{\text{eff}}(x) = \rho(l)\lambda_F$ and $\rho_{c,\text{eff}}(x) = \rho_c(l)\lambda_F$ for the wire.

As can be seen in Fig. 17, the eigenenergies of the QR at $m = -1$ correspond very well to the eigenenergies of a wire with the same parameters. Likewise, the probability and charge densities of the two geometries are very similar with a slight difference in their probability maxima in Fig. 17 (b), which are different for the QR due to the inequivalent inner and outer edge modes, unlike for the wire geometry. The similarity is even more pronounced if instead of the densities $\rho(r)\lambda_F^2$ and $\rho_c(r)\lambda_F^2$ the radial densities $\rho(r)r\lambda_F$ and $\rho_c(r)r\lambda_F$ are chosen. Then, both maxima in the probability density of the QR have the same height similar to the wire.

¹ E. Majorana, *Il Nuovo Cimento* **14**, 171 (1937).

² F. Wilczek, *Nat. Phys.* **5**, 614 (2009).

³ M. Franz, *Physics* **3**, 24 (2010).

⁴ J. Alicea, *Rep. Prog. Phys.* **75**, 076501 (2012).

⁵ M. Leijnse and K. Flensberg, *Semiconductor Science and Technology* **27**, 124003 (2012).

⁶ C. Beenakker, *Annu. Rev. Condens. Matter Phys.* **4**, 113 (2013).

⁷ M. Franz, *Nat. Nanotechnol.* **8**, 149 (2013).

⁸ G. Tkachov and E. M. Hankiewicz, *Phys. Status Solidi B* **250**, 215 (2013).

⁹ C. Nayak, S. H. Simon, A. Stern, M. Freedman, and S. Das Sarma, *Rev. Mod. Phys.* **80**, 1083 (2008).

¹⁰ J. Alicea, Y. Oreg, G. Refael, F. von Oppen, and M. P. A.

Fisher, *Nat. Phys.* **7**, 412 (2011).

¹¹ M. Z. Hasan and C. L. Kane, *Rev. Mod. Phys.* **82**, 3045 (2010).

¹² X.-L. Qi and S.-C. Zhang, *Rev. Mod. Phys.* **83**, 1057 (2011).

¹³ S.-Q. Shen, *Topological insulators: Dirac equation in condensed matters* (Springer, Berlin, 2012).

¹⁴ N. B. Kopnin and M. M. Salomaa, *Phys. Rev. B* **44**, 9667 (1991).

¹⁵ G. Volovik, *J. Exp. Theor. Phys. Lett.* **70**, 609 (1999).

¹⁶ T. Senthil and M. P. A. Fisher, *Phys. Rev. B* **61**, 9690 (2000).

¹⁷ N. Read and D. Green, *Phys. Rev. B* **61**, 10267 (2000).

- ¹⁸ A. Y. Kitaev, *Physics-Uspekhi* **44**, 131 (2001).
- ¹⁹ K. Sengupta, I. Žutić, H.-J. Kwon, V. M. Yakovenko, and S. Das Sarma, *Phys. Rev. B* **63**, 144531 (2001).
- ²⁰ S. Das Sarma, C. Nayak, and S. Tewari, *Phys. Rev. B* **73**, 220502 (2006).
- ²¹ A. P. Mackenzie and Y. Maeno, *Rev. Mod. Phys.* **75**, 657 (2003).
- ²² However, there are also possible alternative scenarios for chiral pairing symmetry [I. Žutić and I. Mazin, *Phys. Rev. Lett.* **95**, 217004 (2005)]. For chiral p -wave symmetry, anomalous terms in the charge and current response have been proposed [R. M. Lutchyn, P. Nagornykh, and V. M. Yakovenko, *Phys. Rev. B* **77**, 144516 (2008)]. We do not consider such terms in this paper, nor a possible nonlinear relation between the superfluid velocity and the supercurrent [K. Halterman and O. T. Valls, *Phys. Rev. B* **62**, 5904 (2000); I. Žutić and O. T. Valls, *Phys. Rev. B* **58**, 8738 (1998)].
- ²³ M. Sato, Y. Takahashi, and S. Fujimoto, *Phys. Rev. Lett.* **103**, 020401 (2009).
- ²⁴ J. D. Sau, R. M. Lutchyn, S. Tewari, and S. Das Sarma, *Phys. Rev. Lett.* **104**, 040502 (2010).
- ²⁵ J. D. Sau, S. Tewari, R. M. Lutchyn, T. D. Stanescu, and S. Das Sarma, *Phys. Rev. B* **82**, 214509 (2010).
- ²⁶ J. Alicea, *Phys. Rev. B* **81**, 125318 (2010).
- ²⁷ I. Žutić, J. Fabian, and S. Das Sarma, *Rev. Mod. Phys.* **76**, 323 (2004).
- ²⁸ J. Fabian, A. Matos-Abiague, C. Ertler, P. Stano, and I. Žutić, *Acta Phys. Slov.* **57**, 565 (2007).
- ²⁹ Proximity-induced superconductivity in topological insulators, however, is argued to require special attention [A. M. Black-Schaffer and A. V. Balatsky, *Phys. Rev. B* **86**, 144506 (2012)] and actually exhibits a mixed s - and p -wave character [G. Tkachov and E. M. Hankiewicz, *Phys. Rev. B* **88**, 075401 (2013)].
- ³⁰ L. Fu and C. L. Kane, *Phys. Rev. Lett.* **100**, 096407 (2008).
- ³¹ R. M. Lutchyn, J. D. Sau, and S. Das Sarma, *Phys. Rev. Lett.* **105**, 077001 (2010).
- ³² Y. Oreg, G. Refael, and F. von Oppen, *Phys. Rev. Lett.* **105**, 177002 (2010).
- ³³ J. Klinovaja, P. Stano, and D. Loss, *Phys. Rev. Lett.* **109**, 236801 (2012).
- ³⁴ A. Cook and M. Franz, *Phys. Rev. B* **84**, 201105 (2011).
- ³⁵ A. M. Cook, M. M. Vazifeh, and M. Franz, *Phys. Rev. B* **86**, 155431 (2012).
- ³⁶ M. Kjaergaard, K. Wölms, and K. Flensberg, *Phys. Rev. B* **85**, 020503 (2012).
- ³⁷ B. Braunecker and P. Simon, *Phys. Rev. Lett.* **111**, 147202 (2013).
- ³⁸ M. M. Vazifeh and M. Franz, *Phys. Rev. Lett.* **111**, 206802 (2013).
- ³⁹ J. Klinovaja, P. Stano, A. Yazdani, and D. Loss, *Phys. Rev. Lett.* **111**, 186805 (2013).
- ⁴⁰ C. C. Tsuei and J. R. Kirtley, *Rev. Mod. Phys.* **72**, 969 (2000).
- ⁴¹ J. H. Ngai, R. Beck, G. Leibovitch, G. Deutscher, and J. Y. T. Wei, *Phys. Rev. B* **82**, 054505 (2010).
- ⁴² J. Linder, Y. Tanaka, T. Yokoyama, A. Sudbø, and N. Nagaosa, *Phys. Rev. Lett.* **104**, 067001 (2010).
- ⁴³ M. Sato, Y. Takahashi, and S. Fujimoto, *Phys. Rev. B* **82**, 134521 (2010).
- ⁴⁴ P. Lucignano, A. Mezzacapo, F. Tafuri, and A. Tagliacozzo, *Phys. Rev. B* **86**, 144513 (2012).
- ⁴⁵ C. C. Tsuei, *ArXiv e-prints* (2013), arXiv:1306.0652.
- ⁴⁶ A. Heimes, P. Kotetes, and G. Schön, *Phys. Rev. B* **90**, 060507 (2014).
- ⁴⁷ M. Leijnse and K. Flensberg, *Phys. Rev. B* **86**, 134528 (2012).
- ⁴⁸ R. W. Reithaler, P. Recher, and E. M. Hankiewicz, *Phys. Rev. Lett.* **110**, 226802 (2013).
- ⁴⁹ P. Högl, A. Matos-Abiague, I. Žutić, and J. Fabian, *ArXiv e-prints* (2015), arXiv:1502.08022.
- ⁵⁰ B. Béri, J. N. Kupferschmidt, C. W. J. Beenakker, and P. W. Brouwer, *Phys. Rev. B* **79**, 024517 (2009).
- ⁵¹ K. Flensberg, *Phys. Rev. B* **82**, 180516 (2010).
- ⁵² M. Wimmer, A. R. Akhmerov, J. P. Dahlhaus, and C. W. J. Beenakker, *New J. Phys.* **13**, 053016 (2011).
- ⁵³ C.-H. Lin, J. D. Sau, and S. Das Sarma, *Phys. Rev. B* **86**, 224511 (2012).
- ⁵⁴ Y. Tanaka, T. Yokoyama, and N. Nagaosa, *Phys. Rev. Lett.* **103**, 107002 (2009).
- ⁵⁵ K. T. Law, P. A. Lee, and T. K. Ng, *Phys. Rev. Lett.* **103**, 237001 (2009).
- ⁵⁶ Y. Asano, Y. Tanaka, and N. Nagaosa, *Phys. Rev. Lett.* **105**, 056402 (2010).
- ⁵⁷ A. R. Akhmerov, J. P. Dahlhaus, F. Hassler, M. Wimmer, and C. W. J. Beenakker, *Phys. Rev. Lett.* **106**, 057001 (2011).
- ⁵⁸ D. Schmeltzer and A. Saxena, *Phys. Rev. B* **86**, 094519 (2012).
- ⁵⁹ S. Tewari, J. D. Sau, V. W. Scarola, C. Zhang, and S. Das Sarma, *Phys. Rev. B* **85**, 155302 (2012).
- ⁶⁰ M. Gibertini, R. Fazio, M. Polini, and F. Taddei, *Phys. Rev. B* **88**, 140508 (2013).
- ⁶¹ S. Valentini, R. Fazio, and F. Taddei, *Phys. Rev. B* **89**, 014509 (2014).
- ⁶² E. Grosfeld and A. Stern, *Proc. Natl. Acad. Sci. USA* **108**, 11810 (2011).
- ⁶³ B. Y. Sun and M. W. Wu, *New J. Phys.* **16**, 073045 (2014).
- ⁶⁴ O. Kashuba and C. Timm, *Phys. Rev. Lett.* **114**, 116801 (2015).
- ⁶⁵ S. Valentini, R. Fazio, V. Giovannetti, and F. Taddei, *Phys. Rev. B* **91**, 045430 (2015).
- ⁶⁶ V. Mourik, K. Zuo, S. M. Frolov, S. R. Plissard, E. P. A. M. Bakkers, and L. P. Kouwenhoven, *Science* **336**, 1003 (2012).
- ⁶⁷ M. T. Deng, C. L. Yu, G. Y. Huang, M. Larsson, P. Caroff, and H. Q. Xu, *Nano Letters* **12**, 6414 (2012).
- ⁶⁸ L. P. Rokhinson, X. Liu, and J. K. Furdyna, *Nat. Phys.* **8**, 795 (2012).
- ⁶⁹ A. Das, Y. Ronen, Y. Most, Y. Oreg, M. Heiblum, and H. Shtrikman, *Nat. Phys.* **8**, 887 (2012).
- ⁷⁰ A. D. K. Finck, D. J. Van Harlingen, P. K. Mohseni, K. Jung, and X. Li, *Phys. Rev. Lett.* **110**, 126406 (2013).
- ⁷¹ S. Nadj-Perge, I. K. Drozdov, J. Li, H. Chen, S. Jeon, J. Seo, A. H. MacDonald, B. A. Bernevig, and A. Yazdani, *Science* **346**, 602 (2014).
- ⁷² Y. Peng, F. Pientka, L. I. Glazman, and F. von Oppen, *Phys. Rev. Lett.* **114**, 106801 (2015).
- ⁷³ E. J. H. Lee, X. Jiang, R. Aguado, G. Katsaros, C. M. Lieber, and S. De Franceschi, *Phys. Rev. Lett.* **109**, 186802 (2012).
- ⁷⁴ D. Bagrets and A. Altland, *Phys. Rev. Lett.* **109**, 227005 (2012).
- ⁷⁵ J. Liu, A. C. Potter, K. T. Law, and P. A. Lee, *Phys. Rev. Lett.* **109**, 267002 (2012).
- ⁷⁶ D. I. Pikulin, J. P. Dahlhaus, M. Wimmer, H. Schomerus,

- and C. W. J. Beenakker, *New J. Phys.* **14**, 125011 (2012).
- ⁷⁷ G. Kells, D. Meidan, and P. W. Brouwer, *Phys. Rev. B* **86**, 100503 (2012).
- ⁷⁸ D. Roy, N. Bondyopadhyaya, and S. Tewari, *Phys. Rev. B* **88**, 020502 (2013).
- ⁷⁹ E. J. H. Lee, X. Jiang, M. Houzet, R. Aguado, C. M. Lieber, and S. De Franceschi, *Nat. Nanotechnol.* **9**, 79 (2014).
- ⁸⁰ E. Prada, P. San-Jose, and R. Aguado, *Phys. Rev. B* **86**, 180503 (2012).
- ⁸¹ D. Rainis, L. Trifunovic, J. Klinovaja, and D. Loss, *Phys. Rev. B* **87**, 024515 (2013).
- ⁸² S. Das Sarma, J. D. Sau, and T. D. Stanescu, *Phys. Rev. B* **86**, 220506 (2012).
- ⁸³ I. Appelbaum, *Appl. Phys. Lett.* **103**, 122604 (2013).
- ⁸⁴ E. Vernek, P. H. Penteado, A. C. Seridonio, and J. C. Egues, *Phys. Rev. B* **89**, 165314 (2014).
- ⁸⁵ G. Ben-Shach, A. Haim, I. Appelbaum, Y. Oreg, A. Yacoby, and B. I. Halperin, *Phys. Rev. B* **91**, 045403 (2015).
- ⁸⁶ M.-T. Rieder, P. W. Brouwer, and I. Adagideli, *Phys. Rev. B* **88**, 060509 (2013).
- ⁸⁷ I. Adagideli, M. Wimmer, and A. Teker, *Phys. Rev. B* **89**, 144506 (2014).
- ⁸⁸ S. Gangadharaiah, B. Braunecker, P. Simon, and D. Loss, *Phys. Rev. Lett.* **107**, 036801 (2011).
- ⁸⁹ E. M. Stoudenmire, J. Alicea, O. A. Starykh, and M. P. Fisher, *Phys. Rev. B* **84**, 014503 (2011).
- ⁹⁰ M. Stone and R. Roy, *Phys. Rev. B* **69**, 184511 (2004).
- ⁹¹ P. Fendley, M. P. A. Fisher, and C. Nayak, *Phys. Rev. B* **75**, 045317 (2007).
- ⁹² C. Benjamin and J. Pachos, *Phys. Rev. B* **81**, 085101 (2010).
- ⁹³ P. Lucignano, F. Tafuri, and A. Tagliacozzo, *Phys. Rev. B* **88**, 184512 (2013).
- ⁹⁴ Rashba spin-orbit coupling at the interface of a normal-metal/*p*- or *d*-wave superconductor junction can also have a profound effect on the tunneling conductance [S.Wu and K. V. Samokhin, *Phys. Rev. B* **81**, 214506 (2010); S.Wu and K. V. Samokhin, *Phys. Rev. B* **82**, 184501 (2010)].
- ⁹⁵ F. Pientka, A. Romito, M. Duckheim, Y. Oreg, and F. von Oppen, *New J. Phys.* **15**, 025001 (2013).
- ⁹⁶ For open boundary conditions, the overlap between Majorana fermions is actually smallest for $p = \sqrt{2}$, where the lowest-order finite-difference scheme corresponds to the special case of the Kitaev chain from Ref. 18 in which perfect Majorana fermions at exactly zero energy are localized at both ends of the chain.
- ⁹⁷ The agreement between the behavior of the charge density in one-dimensional wires detailed in Ref. 85 and in QRs is even more pronounced if the radial charge density $r\rho_c(r) = r[|f(r)|^2 - |g(r)|^2]$ is considered instead of $\rho_c(r)$.
- ⁹⁸ P. G. D. Gennes, *Superconductivity of Metals and Alloys* (Addison-Wesley, Reading, MA, 1989).
- ⁹⁹ For unconventional pairing, components of the magnetic field may have a nonmonotonic dependence and even *increase* away from the surface of a superconductor, within the thickness of the London penetration depth [I. Žutić and O. T. Valls, *J. Comp. Phys.* **136**, 337 (1997)].
- ¹⁰⁰ M. Tinkham, *Introduction to Superconductivity* (McGraw-Hill, New York, 1996).
- ¹⁰¹ Impurity-induced bound states offer a possibility to probe this topological superconductivity [H. Hu, L. Jiang, H. Pu, Y. Chen, and X.-J. Liu, *Phys. Rev. Lett.* **110**, 020401 (2013); J. D. Sau and E. Demler, *Phys. Rev. B* **88**, 205402 (2013)].
- ¹⁰² As is usually done, we use a phenomenological *s*-wave pairing parameter Δ to model the superconducting proximity effect. A more sophisticated treatment, however, requires simultaneously solving the BdG equation and determining the pairing amplitude self-consistently [O. T. Valls, M. Bryan, and I. Žutić, *Phys. Rev. B* **82**, 134534 (2010)]. Moreover, the semiconductor as potential Majorana host has to be in direct contact with the superconductor to induce localized Majorana fermions there [V. Stanev and V. Galitski, *Phys. Rev. B* **89**, 174521 (2014)].
- ¹⁰³ In a ring with an outer radius of $R_o = 10 \mu\text{m}$ but with otherwise similar parameters to Fig. 16, the splitting would be $E_{A/B} \approx \pm 2.7 \times 10^{-8} \text{ eV} \approx \pm 1.0 \times 10^{-4} E_F$.
- ¹⁰⁴ F. W. J. Olver, D. W. Lozier, R. F. Boisvert, and C. W. Clark, *NIST Handbook of Mathematical Functions* (Cambridge Univ. Press, New York, 2010).